

# Properties of Galactic Dark Matter: Constraints from Astronomical Observations

B. Burch<sup>1,2</sup> and R. Cowsik<sup>1</sup>

Physics Department and McDonnell Center for the Space Sciences, Washington University,  
St. Louis, MO, 63130

Received \_\_\_\_\_; accepted \_\_\_\_\_

---

<sup>1</sup>Campus Box 1105, 1 Brookings Drive, St. Louis, MO 63130

<sup>2</sup>bburch@physics.wustl.edu

## ABSTRACT

The distributions of normal matter and of dark matter in the Galaxy are coupled to each other as they both move in the common gravitational potential. In order to fully exploit this interplay and to derive the various properties of dark matter relevant to their direct and indirect detection, we have comprehensively reviewed the astronomical observations of the spatial and velocity distributions of the components of normal matter. We then postulate that the phase-space distribution of dark matter follows a lowered-isothermal form and self-consistently solve Poisson’s equation to construct several models for the spatial and velocity distributions of dark matter. In this paper, we compute the total gravitational potential of the normal and dark matter components and investigate their consistency with current observations of the rotation curve of the Galaxy and of the spatial and velocity distributions of blue horizontal-branch and blue straggler stars. Even with this demand of consistency, a large number of models with a range of parameters characterizing the dark matter distribution remain. We find the best choice of parameters, within the range of allowed values, for the surface density of the disk  $55 \text{ M}_\odot \text{ pc}^{-2}$ , are the following: the dark matter density at the Galactic center  $\rho_{DM,c} \approx 100 - 250 \text{ GeV cm}^{-3}$ , the local dark matter density  $\rho_{DM}(R_0) \approx 0.56 - 0.72 \text{ GeV cm}^{-3}$ , and the root-mean-speed of dark matter particles  $\langle v_{DM}^2(R_0) \rangle^{1/2} \approx 490 - 550 \text{ km s}^{-1}$ . We also discuss possible astronomical observations that may further limit the range of the allowed models. The predictions of the allowed models for direct and indirect detection will be discussed separately in a companion paper.

*Subject headings:* dark matter — Galaxy: fundamental parameters — Galaxy: structure

## 1. Introduction

In the study of dark matter, in its role in the formation of structures in the Universe, and in its direct and indirect detection, the mass and luminosity distribution of the Milky Way Galaxy plays a central role. Such considerations perhaps began with the contributions of Oort (1932) to the understanding of the problem in terms of the mass model of the Milky Way and is still relevant. The importance of dark matter, especially weakly interacting relics from the Big Bang (Cowsik & McClelland 1972, 1973; Lee & Weinberg 1977; Kolb & Turner 1996), in the formation and dynamics of galactic systems became well-established in the decades following the early 1970’s when detailed and critical reviews were written, and modeling of the luminosity distributions and kinematic probes of the Galactic potentials were undertaken (Schmidt 1956; Bahcall & Soneira 1980; Caldwell 1981; Rohlfs & Kreitschmann 1988). Since that time, systematic improvements of the mass models have taken place, notably by Dehnen & Binney (1998), who were concerned with shedding light on the spheroidal nature of the Galactic halo. To this end, they calculated the Galactic gravitational potential for an axisymmetric mass model and investigated its concordance with astronomical constraints obtained from the observations including terminal velocities in the inner Galaxy, the rotation curve, Oort constants, satellites of the Milky Way, the local surface density of the disc (Kuijken & Gilmore 1991), etc. Even though the conceptual basis of the mass models have remained more or less the same, significant sophistication in constraining the parameters of the models, such as Bayesian or Markov Chain Monte-Carlo methods, have led to significant progress (Weber & de Boer 2010; McMillan 2011). With progressively improving capabilities in computation, numerical simulations of galaxy formation provide new mass profiles such as that by Navarro, Frenk, & White (1997), which have provided further stimulus to addressing issues related to the mass models, including forms that avoid the central cusp, which could have been smoothened by baryonic infall (Nesti & Salucci 2013). The phenomenal sensitivities for the direct detection

of the particles of dark matter with instruments placed underground (Aghmet et al. 2011; Aprile et al. 2012; Behnke et al. 2011; Archambault et al. 2012; Felizardo et al. 2012) have brought the focus of these studies to the velocity distribution of the dark matter particles, as this is needed for the proper analysis of the signals detected in these experiments. To this end, several authors have adopted the Eddington formula (Binney & Tremaine 2008), which allows the calculation of the velocity distribution of particles that will self-consistently give rise to a spherically symmetric density distribution that generates the spherically symmetric gravitational potential. By approximating the gravitational potential of the Galaxy to be spherically symmetric, the distribution function that will yield a chosen spherically symmetric mass model for the dark matter halo can be determined (Catena & Ullio 2012; Bhattacharjee et al. 2013). It is clear from this brief review that the development of the mass models has progressed systematically and has reached a high level of sophistication.

With these aforementioned developments, mass models have reached an important watershed. To proceed further one may take recourse to the well-established paradigm in many branches of Physics and Astrophysics and try to specify the form of the phase-space distribution for all the components of the Galaxy, including the dark matter. If this can be achieved, all the quantities of astrophysical interest may be calculated from these distributions. However, this is a far too challenging task at this stage and one must approach the problem in steps. In this paper, we have adopted an alternative approach (Cowsik, Ratnam, & Bhattacharjee 1996) to the modeling of the Galaxy: we start with a functional form for the phase-space distribution of dark matter, which is motivated by physical considerations and has parameters that have a direct bearing on the problem at hand. We then take recourse to astronomical data to obtain a parameterized description of the mass distribution of baryonic (visible) matter in the Galaxy. We then calculate, *self-consistently*, how dark matter with the specified phase-space distribution will distribute itself in the gravitational potential generated by the dark matter itself and that generated



by the visible matter in the Galaxy. Then, the same set of kinematic and other constraints derived from astronomical observations used in constraining the mass models is used to derive the parameters of the phase-space distribution. This approach has not been used extensively, but the earlier studies have indicated some benefits to having a physically motivated distribution function on hand to address the problems related to direct and indirect detection of dark matter. Even this restricted approach already allows us to estimate, for example, the allowed range of the dark matter densities in the central regions of the Galaxy, a parameter difficult to obtain from other methods which rely exclusively on the kinematic indicators like dispersion of the bulge stars and rotation curves in the central regions of the Galaxy, which are dominated by the visible matter distributions in those regions. The phase-space distribution is the same throughout the Galaxy and as such, can efficiently probe the properties of the system in the entire region accessed by the dynamical trajectories.

As stated above, though the precise phase-space distribution of Galactic dark matter is still not well understood, much effort has been invested in understanding the distribution and dynamics of dark matter in the Milky Way for the purposes of understanding the overall dynamics and structure of our Galaxy as well as for the planning and interpretation of their direct and indirect detection. Most studies assume the framework of the Standard Halo Model of dark matter, which envisages the Milky Way as embedded in an isothermal dark matter halo described by a Maxwell-Boltzmann phase-space distribution (often without ensuring self-consistency) with a local dark matter density of  $0.3 \text{ GeV cm}^{-3}$  and a velocity dispersion of  $270 \text{ km s}^{-1}$ , and the radial distribution of its density is truncated at the “virial radius” to keep the mass of the halo and the escape velocity finite. However, it is well understood that a Maxwellian distribution is not appropriate for the description of Galactic dark matter (Kuhlen 2010), as it leads to infinite spatial extent and a total mass for the system that indefinitely increases linearly at large distances. Also, recent attempts

to estimate the local dark matter density leads to a wide range of values  $\sim 0.2 - 0.6 \text{ GeV cm}^{-3}$ :  $\sim 0.39 \text{ GeV cm}^{-3}$  (Catena & Ullio 2010),  $0.2\text{-}0.4 \text{ GeV cm}^{-3}$  (Weber & de Boer 2010),  $0.40 \pm 0.04 \text{ GeV cm}^{-3}$  (McMillan 2011),  $0.43 \pm 0.11 \pm 0.10 \text{ GeV cm}^{-3}$  (Salucci et al. 2010),  $0.3 \pm 0.1 \text{ GeV cm}^{-3}$  (Bovy & Tremaine 2012). In this paper, we carry out a self-consistent calculation of the spatial distribution of dark matter, including the effects of the background gravitational potential generated by the baryonic matter in the Galaxy. Comparison of the predictions of the self-consistent model with various kinematic observables constrain the parameters characterizing the phase-space distribution of Galactic dark matter. This allows us to derive the density distribution and other properties pertaining to Galactic dark matter particles in a self-consistent way.

We follow the basic strategy for probing the phase-space distribution (PSD) of dark matter developed by Cowsik, Ratnam, & Bhattacharjee (1996). The distributions of dark matter and visible matter are coupled to each other as they are both influenced by the common gravitational potential of the Galaxy, to which each component makes its own contribution. Thus, when we have at hand the density distribution of visible matter, determined by astronomical observations, it is a straight-forward matter to calculate the gravitational potential generated by visible matter. Then, for any assumed functional form for the PSD of dark matter, with a given a set of parameters, we can solve the non-linear Poisson equation to determine the potential contributed by dark matter. Thus, having determined the total potential of the Galaxy, we may then use astronomical probes like the rotation curve of the Galaxy and the velocity and spatial distribution of stars to determine the values of the parameters characterizing the PSD function of dark matter that provide good fit to these observations.

The accuracy of determination of the parameters characterizing the phase-space distribution of Galactic dark matter depends primarily on the accuracy and extent of

astronomical data. Accordingly, the observations of the distribution of the various visible mass components of the Milky Way are reviewed in detail, and correspondingly, a simple axisymmetric model of the density distribution of the Galactic stars and gas is constructed. The particles of dark matter move in the gravitational potential generated by the visible matter and by their own mass distribution, and their spatial distribution is generally assumed to be cut off at the “virial radius”, defined as the radius of a sphere which has an average density of  $\Delta$  times the critical density. The value of  $\Delta$  suggested by different authors ranges from  $\Delta = 200$  (McMillan 2011) to  $\Delta = 355$  (Libeskind 2010) or more. However, our analysis indicates that many of the parameters of the phase-space distribution function of dark matter are only weakly sensitive to this choice. Assuming a lowered-isothermal phase-space distribution for Galactic dark matter, the gravitational potential from dark matter is computed from iterative, self-consistent, solutions of Poisson’s equation, following a method adopted by Cowsik, Ratnam, & Bhattacharjee (1996). In this way, many dark matter profiles are generated with a wide range of properties depending on the choice of the parameters specifying their PSD. These models are then compared in turn with the current observations of the Galactic rotation curve and to recent observations of the velocity and spatial distribution of blue horizontal-branch (BHB) and blue straggler (BS) stars in the outer Galaxy. Comparing the dark matter models with the rotation curve and with the BHB/BS distributions separately allows for a wide range of dark matter properties. On the other hand, when we demand that the models fit both these simultaneously for the same choice of parameters, the parameter space narrows and becomes almost exclusively dependent on the value chosen for the surface density and scale lengths of the visible disk of the Galaxy. However, even in the combined analysis of the rotation curve and the stellar distributions, a significant range of parameters for the phase-space distribution of dark matter is still allowed. Within the current estimates of the mass of the Galactic disk, we find that the best estimates for the local dark matter density are  $\sim 0.56\text{--}0.72 \text{ GeV cm}^{-3}$

with the value of the density at the Galactic center ranging from 100-250  $\text{GeV cm}^{-3}$ . The escape speed from the center of the Galaxy lies in the range  $\sim 940 - 980 \text{ km s}^{-1}$ , and the root-mean-square speed of dark matter particles in the Solar neighborhood is found to be  $\sim 490\text{-}550 \text{ km s}^{-1}$  for the most favored models.

## 2. The Visible Matter Distribution

In order to derive the Galactic dark matter distribution, the distribution of visible matter in the Galaxy must be well understood, as it is their interplay that allows us to probe the dark matter. We have completed an extensive survey of the current observations of the distributions of stars and gas in the Milky Way and constructed a simple axisymmetric model of the Galaxy that agrees with current data. The known mass distribution of the Galaxy derives contributions from the central black hole, central bulge, disk, and stellar halo populations. In this analysis, the stellar halo is neglected because its contribution to the visible matter density is on the order of 0.1% at  $R_0$ , the distance from the Sun to the Galactic center (Helmi 2008), and it is therefore expected to contribute negligibly to the dynamics of the Galaxy. Likewise, the black hole and nuclear bulge, whilst playing important roles very close to the Galactic center, contribute negligibly to the overall dynamics of the Galaxy in the regions of interest. For the purposes of computing the gravitational potential in this paper, the visible Galaxy consists of a central bulge and a thin and a thick exponential disk. There are several ways to model these components, and here, models that most closely fit the observations of the stars and gas are adopted.

## 2.1. The Disk

The mass density of both the thin (tn) and the thick (tk) disk components are typically modeled as double-exponential functions with early evidence for their validity given by Freeman (1970). Following the notation used in many recent analyses (Cabrera-Lavers et al. 2005; McMillan 2011), the densities for the separate components may be written as,

$$\rho_{tn}(r, z) = \frac{\Sigma_{tn,c}}{2z_{tn}} e^{-|z|/z_{tn}} e^{-r/r_{tn}}, \quad (1)$$

$$\rho_{tk}(r, z) = \frac{\Sigma_{tk,c}}{2z_{tk}} e^{-|z|/z_{tk}} e^{-r/r_{tk}}, \quad (2)$$

$$\rho_d = \rho_{tn} + \rho_{tk}, \quad (3)$$

$$\Sigma_d = \Sigma_{tn} + \Sigma_{tk}, \quad (4)$$

in cylindrical coordinates, where  $\rho_d$  is the total density of the Galactic disk,  $\Sigma_{tk/tn,c}$  are the surface densities near the Galactic center (including both stars and gas),  $z_{tk/tn}$  are the scale heights, and  $r_{tk/tn}$  are the radial scale lengths for the thick and thin components respectively. The masses of the two components are given by

$$M_{tk/tn} = 2\pi \Sigma_{tk/tn,c} r_{tk/tn}^2. \quad (5)$$

For the total local surface density at  $R_0$  from visible matter, we consider the values  $\Sigma_{d,\odot} = 40, 55$ , and  $70 \text{ M}_\odot \text{ pc}^{-2}$ , which is within the range found in the literature (Kuijken & Gilmore 1989, 1991; Flynn & Fuchs 1994; Gould et al. 1996; Korchagin 2003; Siebert 2003; Holmberg & Flynn 2004; Flynn 2006; Weber & de Boer 2010). For convenience, the ratio of the thick disk surface density at  $R_0$  to the total surface density at  $R_0$  is taken to be

$$\frac{\Sigma_{tk,\odot}}{\Sigma_{tk,\odot} + \Sigma_{tn,\odot}} = 0.1, \quad (6)$$

a value that is also within the range of the findings of many studies (Ohja 2001; Reid & Majewski 1993; Buser et al. 1999; Spagna 1996; Ng et al. 1997; Larsen & Humphreys 2003; Robin et al. 1996; Siegel et al. 2002; Carollo et al. 2010). The choice of the ratio in eq. 6,

within observational constraints, does not have a significant effect on the rotation curve or other dynamical indicators calculated in this paper.

From the compilation of observations, a complete range in the radial scale length of the thin disk  $r_{tn}=2.0, 2.5, 3.0$ , and  $3.5$  kpc was considered, and  $r_{tk}$  was taken to be  $3.5$  kpc, though there is recent evidence that the radial scale length of the thick disk could be as short as  $\sim 2$  kpc (Bensby et al. 2011; Cheng et al. 2012; Bovy et al. 2012a). The scale heights are chosen to be  $z_{tn} = 350$  pc and  $z_{tk} = 900$  pc, close to the values determined by Jurić et al. (2008) and are seen to not have a strong effect on the calculated rotation curve, agreeing with the analysis of McMillan (2011). The above parameters yield a combined disk mass in the range  $3.57 - 6.24 \times 10^{10} M_{\odot}$ . Note, this simple disk model does not include some of the finer structures of the disk such as the spiral arms or the warp included in other analyses (Sofue et al. 2009) since an axisymmetric model is adequate to describe the overall dynamics and accords computational simplicity.

The disk potential has the form (Kuijken & Gilmore 1989; Mo et al. 2010)

$$\begin{aligned} \Phi_d(r, z) = & -2\pi G \left( \Sigma_{tn, c} r_{tn}^2 \int_0^\infty dk \frac{J_0(kr)}{[1 + (kr_{tn})^2]^{3/2}} \frac{e^{-k|z|} - (kz_{tn})e^{-|z|/z_{tn}}}{1 - (kz_{tn})^2} \right. \\ & \left. + \Sigma_{tk, c} r_{tk}^2 \int_0^\infty dk \frac{J_0(kr)}{[1 + (kr_{tk})^2]^{3/2}} \frac{e^{-k|z|} - (kz_{tk})e^{-|z|/z_{tk}}}{1 - (kz_{tk})^2} \right). \end{aligned} \quad (7)$$

Note the potential includes integration over Bessel functions,  $J_0(kr)$ , which slows down numerical calculations of the rotation curve for the different models. We find that using an adaptive quasi-Monte Carlo method in *Mathematica* provides the quickest computation time without sacrificing accuracy.

## 2.2. The Bulge

The bulge, in cylindrical coordinates, is described by a Plummer density profile of the form

$$\rho_b = \frac{3M_b}{4\pi b^3} \left( 1 + \frac{r^2 + z^2}{b^2} \right)^{-5/2}, \quad (8)$$

where  $M_b$  is the total mass of the bulge and  $b$  is the scale radius. To determine  $M_b$  and  $b$ , we assume the dark matter contribution to the dynamics from  $\sim 0.1 - 1$  kpc is small (an assumption that implies that visible matter dominates the dynamics in the very central regions of the Galaxy and is justified *post facto*) and subtract the disk contribution from the inner 1 kpc. Noting that the contributions of various components to  $v_c^2(r)$  are additive, we subtract the theoretically expected contribution to  $v_c^2(r)$  from the square of the observed values for  $r \lesssim 1$  kpc to obtain the exclusive contribution of the bulge. The resulting points are fit with the rotation curve derived from the Plummer density. The bulge parameters are found to be  $M_b = 1.02 \times 10^{10} M_\odot$  and  $b = 0.258$  kpc. The potential of the Plummer model has the simple analytical form

$$\Phi_b = -\frac{GM_b}{(r^2 + z^2 + b^2)^{1/2}} \quad (9)$$

and a velocity dispersion (Dejonghe 1987) given by

$$\sigma_b^2 = \frac{GM_b}{6(r^2 + z^2 + b^2)^{1/2}}. \quad (10)$$

We show the velocity dispersion in Fig. 1, along with measurements of K and M bulge giants (Minniti 1992; Rich et al. 2007; Blum et al. 1995). Note that the dispersion expected from the Plummer model agrees well with the observations, implying that this region is adequately described by a bulge-dominated density profile. Including the mass contribution from the disk in the bulge region does not noticeably change the predictions for the velocity dispersion.

### 3. Kinematic Observations: The Rotation Curve and Stellar Velocity Distributions

Recent observations of stars, interstellar gas, and masers have been able to extend our understanding of the dynamics of the Galaxy beyond the Solar circle as well as improving observations near the Solar location. The density and dynamics of these objects probe the Galactic gravitational potential. The gravitational potential in the Galactic plane as a function of the distance from the Galactic center can be determined from the rotational speed of the Galaxy in the usual way:

$$\frac{v_c^2}{r} = \left| \frac{\partial \Phi_{tot}}{\partial r} \right|, \quad (11)$$

where  $\Phi_{tot}$  is the total gravitational potential of the Galaxy, obtaining contributions from both its visible and dark matter components. The best observations of the Milky Way’s rotation curve now span the range of galactocentric distances  $\sim 1 - 20$  kpc. The Galactic potential can be probed up to  $\sim 90$  kpc by considering the velocity distribution of BHB and BS stars. Recent compilations of carefully selected BHB stars by Xue et al. (2008) and BHB and BS stars by Brown et al. (2010) are used below to constrain the Galactic dark matter distribution.

#### 3.1. The Rotation Curve

The best estimates of the gravitational potential in the Galactic plane within  $\sim 10$  kpc of the Galactic center come from measurements of the Galactic rotation speed. We have compiled a large sample of the available observations (Burton & Gordon 1978; Blitz et al. 1982; Schneider & Terzian 1983; Clemens 1985; Fich et al. 1989; Burton & Liszt 1993; Turbide & Moffat 1993; Honma & Sofue 1997; Pont et al. 1997; Honma et al. 2007; McClure-Griffiths & Dickey 2007; Oh et al. 2010; Stepanishchev & Bobylev 2011), excluding



only those with exceptionally high dispersion in the data (Demers & Battinelli 2007). The rotation curve inside the solar circle is well-determined by observations of HI regions and CO emission associated with HII regions. Outside the solar circle, distances to objects are much more difficult to measure accurately, so the errors in the rotation curve are correspondingly larger. We present a compilation of the data used in our analysis in Fig. 2, with error bars when available, along with a medial shaded band, which includes 2/3 of the data points in 1 kpc radial bins and the rotation curve from the visible components of our Galactic mass models with  $r_{tn} = 3$  kpc.

The Milky Way’s rotation curve is derived from line-of-sight observations of interstellar hydrogen and other material like CO, masers, planetary nebula, and other astrophysical objects. The determination of the rotation curve of the Galaxy depends on the assumed value of  $R_0$ , the distance from the Galactic center to the Sun and  $\Theta_0$ , the rotation speed of the Sun about the Galactic center. Recently, maser observations and measurements of stellar orbits near SgrA\* have been able to constrain  $R_0 = 7.2 - 9$  kpc (Ghez et al. 2008; Gillessen et al. 2009; Reid 2009; Reid et al. 2008; Brunthaler et al. 2011). A summary of some estimates of  $R_0$  can be found in Avedisova (2005). We choose  $R_0 = 8.3$  kpc based on these and other stellar observations from the past decade. The ratio  $\Theta_0/R_0$  is well constrained from masers and stellar orbits (Reid 2009; Brunthaler et al. 2011; Reid & Brunthaler 2004) and is in the range of  $\Theta_0/R_0 = 28.5 - 30.3$  km s<sup>-1</sup> kpc<sup>-1</sup>. We take  $\Theta_0/R_0 \approx 28.9$  km s<sup>-1</sup> kpc<sup>-1</sup> such that  $\Theta_0 = 240$  km s<sup>-1</sup>. This value of  $\Theta_0$  differs significantly from the IAU standard values (see McMillan & Binney (2010) and the references therein) of  $R_0 = 8.5$  kpc and  $\Theta_0 = 220$  km s<sup>-1</sup>, which gives  $\Theta_0/R_0 \approx 25.9$  km s<sup>-1</sup> kpc<sup>-1</sup> and does not agree with the recent observations of masers and stellar orbits. There are, however, some recent studies which call into question this high value of  $\Theta_0$  (Koposov et al. 2010; Bovy et al. 2012b), preferring values closer to 220 km s<sup>-1</sup>. The result of reanalyzing the observations using the larger value of  $\Theta_0$  is that the rotation curve gently rises from  $\sim 2 - 15$  kpc instead

of remaining flat, and correspondingly, the density of dark matter needed to reconcile the theoretically computed rotation curve with the data increases. We have also corrected all the rotation curve data taking account of the new measurements of the peculiar motion of the Sun ( $U_{\odot}, V_{\odot}, W_{\odot}$ ), where  $V_{\odot}$  has been updated from  $\sim 5 \text{ km s}^{-1}$  to  $\sim 11 - 15 \text{ km s}^{-1}$  (McMillan & Binney 2010; Schönrich et al. 2010). We take  $(U_{\odot}, V_{\odot}, W_{\odot}) = (11, 12, 7.5) \text{ km s}^{-1}$ .

### 3.2. Blue Horizontal-Branch Stars

Xue et al. (2008) have compiled an extensive list of the line-of-sight velocities of 2401 BHB stars from the Sloan Digital Sky Survey DR6 taking care to ensure their sample is pure and contains accurate data on both the distance and line-of-sight velocity of each star. They use this data to constrain cosmological simulations and estimate the virial mass of the Galaxy as well as derive the rotation curve up to  $\sim 60 \text{ kpc}$ . We combine their compilation of 2401 BHB stars within  $60 \text{ kpc}$  of the Galactic center with their separate compilation of stars at galactocentric distances of  $\sim 60 - 90 \text{ kpc}$ . This combined compilation extends from  $5\text{-}90 \text{ kpc}$  with line-of-sight velocities spanning  $\pm 350 \text{ km s}^{-1}$ . After rescaling the galactocentric distances and line-of-sight velocities for each star to correspond to the values of  $R_0$  and  $\Theta_0$  chosen above, the observations are divided into eleven radial bins where the positive and negative radial velocities are averaged and divided into  $50 \text{ km s}^{-1}$  bins. Error bars are shown as  $\pm\sqrt{N}$  where  $N$  is the average number of stars in each velocity bin.

Brown et al. (2010) have compiled a sample of 910 BHB and BS stars from the Hypervelocity Star Survey, which contains twice as many stars at  $r \geq 50 \text{ kpc}$  compared to the compilations by Xue et al., and they derive the velocity dispersion profile of the Milky Way out to  $\sim 95 \text{ kpc}$ . While the Brown et al. sample claims to be complete in color, magnitude depth, and spatial coverage, there is some ambiguity in distinguishing BHB

from BS stars. To achieve the ratio of BHB to BS stars as stated in Brown et al., stars with  $f_{BHB} \geq 0.6$  were taken to be BHB stars, where  $f$  is the likelihood of a candidate star being a BHB star as reported in Table 1 of Brown et al., and any star with  $f_{BHB} < 0.6$  was considered to be a BS star. This reproduces the 74% to 26% BHB to BS ratio in Brown et al. As with the stars in the compilation by Xue et al., this sample too was rescaled for our adopted values of  $R_0$  and  $\Theta_0$ . We find that we are unable to reproduce the  $R_{BHB}$  and  $R_{BS}$  distances in Table 1 of Brown et al. (2010) for their choice of  $R_0$ ,  $\Theta_0$  and  $(U_\odot, V_\odot, W_\odot)$ . We calculate the heliocentric distance for the BHB and BS stars using eq. 2 in Brown et al. and convert it to a galactocentric distance in the usual way (see eq. 4 in Xue et al. (2008)). The stellar observations are then divided into eight radial bins. The line-of-sight velocities are averaged, and the error bars are determined in the same manner as for the Xue et al. distribution.

#### 4. The Galactic Dark Matter Distribution

The density distribution of dark matter is controlled by both the velocity distribution of the dark matter particles and by the total gravitational potential  $\Phi_{tot}$  in which they reside. The total potential receives contributions from the density distributions of both the visible and the dark matter components of the Galaxy:

$$\Phi_{tot} = \Phi_b + \Phi_d + \Phi_{DM}, \quad (12)$$

where  $\Phi_b$ ,  $\Phi_d$ , and  $\Phi_{DM}$  are the potentials contributed by the bulge, the disk, and the dark matter. In order to develop a self-consistent model for the dark matter in our Galaxy, we require a dynamical model whose phase-space distribution function represents a collisionless system that can be parameterized by the velocity dispersion of the dark matter, the density at either the Galactic center or at  $R_0$ , and the size of the dark matter halo. A lowered isothermal (King) distribution is well suited for this and is described in Binney

& Tremaine (2008). Unlike the isothermal sphere, the King distribution has a finite total mass, a non-singular central density, and meets all the requirements of the model. Reasons for choosing the King distribution are also discussed in earlier papers (Cowsik et al. 2007; Chaudhury et al. 2010).

The distribution function for the King model is given by

$$f_K(\varepsilon) = \begin{cases} \frac{\rho_1}{(2\pi\sigma_{DM}^2)^{3/2}} \left( e^{\varepsilon/\sigma_{DM}^2} - 1 \right) & \text{for } \varepsilon > 0 \\ 0 & \text{for } \varepsilon \leq 0 \end{cases} \quad (13)$$

where

$$\varepsilon \equiv \Phi_0 - \left( \frac{1}{2}v^2 + \Phi_{tot} \right). \quad (14)$$

The parameter  $\Phi_0$  is the potential at  $r = r_t$ , the “virial” (King) radius of the dark halo, and  $\rho_1$  and  $\sigma$  are parameters that are related but not equal to the central dark matter density  $\rho_{DM,c}$  and the dark matter velocity dispersion.

The dark matter density distribution is readily calculated by integrating the distribution function

$$\rho_{DM} = \int f_K d^3v \quad (15)$$

and vanishes at  $r = r_t$  where  $\varepsilon = 0$ . Defining the scaled potential  $\Psi(r, z)$  as

$$\Psi(r, z) \equiv \Phi_0 - \Phi_{tot}(r, z), \quad (16)$$

the density distribution of dark matter may be written as

$$\begin{aligned} \rho_{DM}(\Psi(r, z)) &= \frac{\rho_1}{(2\pi\sigma_{DM}^2)^{3/2}} \int_0^{\sqrt{2\Psi(r, z)}} dv v^2 \left[ \exp \left( \frac{\Psi(r, z) - \frac{1}{2}v^2}{\sigma_{DM}^2} \right) - 1 \right] \\ &= \rho_1 \left[ e^{\Psi(r, z)/\sigma_{DM}^2} \text{erf} \left( \frac{\sqrt{\Psi(r, z)}}{\sigma_{DM}} \right) - \sqrt{\frac{4\Psi(r, z)}{\pi\sigma_{DM}}} \left( 1 + \frac{2\Psi(r, z)}{3\sigma_{DM}^2} \right) \right]. \end{aligned} \quad (17)$$

Note that  $\sqrt{2\Psi(r, z)}$  is just the escape speed from the Galaxy of particles at  $(r, z)$ .

Keeping in mind that  $\rho_{DM}$ , which is the source for  $\Phi_{DM}$ , depends on  $\Phi_{DM}$  itself, the dark matter potential must be calculated iteratively by numerically solving the Poisson equation,

$$\nabla^2 \Phi_{DM}(r, z) = 4\pi G \rho_{DM}(r, z), \quad (18)$$

with  $\rho_{DM}(r, z)$  given by eq. 17. The procedure that we adopt here is a Legendre polynomial expansion as described in Cowsik, Ratnam, & Bhattacharjee (1996), which is based on the earlier work by Wilson (1975) and Prendergast & Tomer (1970). In this way, we produce the density and gravitational potential for visible matter and dark matter separately as well as for the sum of the two components.

For the above calculations, we formulate the King distribution in terms of  $\sigma_{DM}$ ,  $\rho_{DM,c}$ , and  $\Psi_0/\sigma_{DM}^2$ , where  $\Psi(r=0, z=0) = \Psi_0$ . The precise choices for  $\sigma$ ,  $\rho_{DM,c}$ , and  $\Psi_0/\sigma_{DM}^2$  are made after solving eq. 18 for a range of values, calculating the corresponding rotation curve (eq. 19), and comparing the results to the observations of the rotation curve and the velocity distribution of BHB and BS stars.

## 5. Comparison with Astronomical Observations

In order to compare model predictions with the observed rotation curve and the observations of spatial and velocity distributions of BHB and BS stars, a large sample of possible dark matter models was generated, with values chosen by hand, encompassing  $\rho_{DM,c} = 1 - 1000 \text{ GeV cm}^{-3}$  (We consider 1, 5, 10, 25, 50, 75, 100, 250, 500, and 1000  $\text{GeV cm}^{-3}$ .),  $\sigma_{DM} \approx 100 - 1000 \text{ km s}^{-1}$  (in 5  $\text{km s}^{-1}$  intervals), and  $\Psi_0/\sigma_{DM}^2 \approx 1 - 25$  (in unit intervals) for each of the twelve disks models. For each model,  $\Psi(r, z)$ ,  $\rho_{DM}(R_0)$ ,  $< v_{DM}^2(R_0) >^{1/2}$ ,  $v_c(R_0)$ , the escape velocity  $v_{esc}$ , and the total mass of the Galaxy  $M_{Galaxy}$  are calculated. Bounds were first put on the parameters of the models by placing the constraint  $220 \text{ km s}^{-1} \leq v_c(R_o) \leq 260 \text{ km s}^{-1}$ . Then, models which agreed with the rotation

curve were found within these bounds.

### 5.1. Comparison with the Rotation Curve

The very discovery of dark matter in the Galaxy and the subsequent determinations of its characteristics rest almost exclusively on the measurements of the rotation curve. In this section, we compare the sequence of models that we have calculated with our compilation of observations shown in Fig. 2 to limit the range of parameters characterizing the phase-space distribution function of dark matter. The theoretical estimates of the rotational velocities are calculated using the expression

$$v_c(r) = \left( r \frac{\partial \Phi_{tot}(r, 0)}{\partial r} \right)^{1/2} = \left( r \frac{\partial}{\partial r} [\Phi_b(r, 0) + \Phi_d(r, 0) + \Phi_{DM}(r, 0)] \right)^{1/2} \quad (19)$$

for the twelve sets of models characterized by the three choices of  $\Sigma_{d,\odot} = 40 \text{ M}_\odot \text{ pc}^{-2}$ ,  $55 \text{ M}_\odot \text{ pc}^{-2}$ , and  $70 \text{ M}_\odot \text{ pc}^{-2}$  and the four choices of  $r_{tn} = 2.0 \text{ kpc}$ ,  $2.5 \text{ kpc}$ ,  $3 \text{ kpc}$ , and  $3.5 \text{ kpc}$ . We display in Tables 1-7 the parameters characterizing the dark matter distribution that fit the rotation curve. We show in Fig. 3 a selection of better fitting models for the rotation curve (i.e. pass through the shaded band) for each these sets of model. The corresponding density profiles for these models are shown in Fig. 4. The local and central dark matter density, the escape velocity from the  $R_0$  and from the Galactic center, and the root-mean-square velocity at  $R_0$  for each of these models are also presented in Tables 1-7.

The following points may be noted after a perusal of the figures and tables:

1. None of the dark matter models were found to be consistent with the rotation curve for a thin disk scale length of 2.0 kpc. For all choices of PSD parameters, the calculated rotation curves were less than  $220 \text{ km s}^{-1}$  at  $R_0$ . To be consistent with the rotation curve, a visible disk with  $r_{tn}=2.0 \text{ kpc}$  would have to have a local surface

density that falls outside observational constraints. For  $r_{tn} = 2.5$  kpc, only the lightest disk produced dark matter models consistent with the rotation curve.

2. All the models presented in Tables 1-7 provide good fits to the observed rotation curve within the solar circle ( $r < R_0$ ).
3. The larger the assumed value of the surface density of the disk, larger is the range of allowed parameters of the dark matter distributions.
4. The range in the parameters allowed by all the various models that best fit the rotation curve is:

- (a)  $872.1 \text{ km s}^{-1} \lesssim v_{esc}(0) \lesssim 983.9 \text{ km s}^{-1}$
- (b)  $506.3 \text{ km s}^{-1} \lesssim v_{esc}(R_0) \lesssim 705.0 \text{ km s}^{-1}$
- (c)  $25 \text{ GeV cm}^{-3} \lesssim \rho_{DM,c} \lesssim 500 \text{ GeV cm}^{-3}$
- (d)  $0.395 \text{ GeV cm}^{-3} \lesssim \rho_{DM}(R_0) \lesssim 0.760 \text{ GeV cm}^{-3}$
- (e)  $392.2 \text{ km s}^{-1} \lesssim \langle v_{DM}^2(R_0) \rangle^{1/2} \lesssim 546.1 \text{ km s}^{-1}$
- (f)  $0.61 \times 10^{12} \text{ M}_\odot \lesssim M_{Galaxy} \lesssim 2.00 \times 10^{12} \text{ M}_\odot$ .

5. Even though we plan to discuss elsewhere the implications of these results for direct and indirect detection of dark matter, we may note here that the range in expected signals is large and the local dark matter density for every model is greater than the standard IAU value of  $0.3 \text{ GeV cm}^{-3}$ . However an assumption of a lower value of  $\Theta_0$  would lead to a lower expectation for the dark matter density. The signals for direct detection are directly proportional to  $\rho_{DM}(R_0)$  and increase at least linearly with  $\langle v_{DM}^2(R_0) \rangle^{1/2}$ , so that the allowed rate may vary at least by  $\sim 8$ , even for detectors with very low threshold. The indirect experiments focus usually on detecting annihilation or decay of dark matter from the central regions of the Galaxy. These rates, proportional to  $\rho_{DM}^2(0)$  and  $\rho_{DM}(0)$ , span a range of 400 and 20 respectively.

6. To investigate the correlations among the various parameters and derived quantities of the dark matter models given in Tables 1-7, the values of  $\sigma_{DM}$ ,  $\langle v_{DM}^2(R_0) \rangle^{1/2}$ ,  $\rho_{DM}(R_0)$ ,  $v_{esc}(0)$ , and  $v_{esc}(R_0)$  are plotted as a function of the central dark matter density,  $\rho_{DM,c}$ , in Figs. 5a-e. Also shown is the dark matter density in the Solar neighborhood as a function of  $\langle v_{DM}^2(R_0) \rangle^{1/2}$  in Fig. 5f. The following observations may be made:

- (a) The correlation between the central density  $\rho_{DM,c}$  and the value of the  $\sigma_{DM}$  parameter is shown in Fig. 5a., and the value of  $\sigma_{DM}$  is shown to decrease with increasing  $\rho_{DM,c}$ . The decrease becomes progressively more gentle, and  $\sigma_{DM}$  reaches a values of  $\sim 195 \text{ km s}^{-1}$  at  $\rho_{DM,c} = 500 \text{ GeV cm}^{-3}$ .
- (b) The root-mean-square velocities of the dark matter particles near the Solar system,  $\langle v_{DM}^2(R_0) \rangle^{1/2}$ , decreases with respect to  $\rho_{DM,c}$  as shown in Fig. 5b.
- (c) Similarly, the dark matter density at  $R_0$  decreases gently with respect to  $\rho_{DM,c}$  as shown in Fig. 5c.
- (d) The escape velocity from the center of the Galaxy and from the location of the solar system gently decreases beyond  $\rho_{DM,c} \sim 200 \text{ GeV cm}^{-3}$  for a given set of disk parameters (see Figs. 5d and 5e).
- (e) The value of  $\rho_{DM}(R_0)$  increases statistically with increasing  $\langle v_{DM}^2(R_0) \rangle^{1/2}$  as shown in Fig. 5f, thereby increasing the range of expectation of event rates in direct detection experiments.

7. After solving Poisson's equation, the potential at every point in the Galaxy is known. It is therefore possible to calculate the force profile in any direction. In Fig. 6, the vertical force profile at the Solar location is shown for a selection of the dark matter models which provide a good fit the observations of the rotation curve. With more extensive astronomical observations, the motions of stars above the Galactic plane



at  $R_0$  could be used to further constrain the dark matter parameters and the surface density of the disk in the neighborhood of the Sun.

## 5.2. Comparison with the Distributions of BHB and BS Stars

The BHB and BS stars, with their distribution extending up to  $\sim 90$  kpc, serve as tracers of the gravitational potential of the Galaxy, even though they contribute negligibly to the potential. Since only their radial velocities are well determined, we will first write down their radial distribution function under the assumption that their PSD function follows the King distribution such as that given in eq. 13. This is achieved by writing  $\Psi(r) = \frac{1}{2}v_{esc}^2(r)$  and integrating the PSD function over the transverse velocities:

$$F_B(r, v_r) = \frac{\rho_B}{(2\pi\sigma_B^2)^{3/2}} \int_0^{v_{esc}^2(r)-v_r^2} \left[ \exp\left(\frac{v_{esc}^2(r) - v_r^2 - v_\perp^2}{2\sigma_B^2}\right) - 1 \right] \pi dv_\perp^2 \quad (20)$$

$$= \frac{\pi\rho_B}{(2\pi\sigma_B^2)^{3/2}} \left\{ 2\sigma_B^2 \left[ \exp\left(\frac{v_{esc}^2(r) - v_r^2}{2\sigma_B^2}\right) - 1 \right] - (v_{esc}^2(r) - v_r^2) \right\} dv_r. \quad (21)$$

The expression given in eq. 21 is suitable for comparison with the observed distributions. However, the samples of BHB and BS stars (Xue et al. 2008; Brown et al. 2010) appear to be incomplete, at least with regard to radial sampling. In order to assess this, we integrate  $F_B(r, v_r)$  over the radial velocities to get the radial distribution of number density, which is given by

$$n_B(r) = \int_0^{v_{esc}(r)} F_B(r, v_r) dv_r \quad (22)$$

$$= \frac{\rho_B}{(2\pi\sigma_B^2)^{3/2}} \left[ \frac{(2\pi\sigma_B^2)^{3/2}}{2} e^{v_{esc}^2(r)/2\sigma_B^2} \operatorname{erf}\left(\frac{v_{esc}(r)}{\sqrt{2\sigma_B^2}}\right) - \frac{2\pi}{3} v_{esc}^3(r) - 2\pi\sigma_B^2 v_{esc}(r) \right] \quad (23)$$

The number of stars in unit radial interval at  $r$  is then given by

$$N(r) = 4\pi r^2 n_B(r). \quad (24)$$

The distributions of BHB and BS stars with  $\sigma_B = 106 \text{ km s}^{-1}$  for the Xue et al. (2008) BHB stars and  $\sigma_B = 115 \text{ km s}^{-1}$  for the Brown et al. (2010) BHB and BS stars calculated for the best fitting model with  $\Sigma_{d,\odot} = 55 \text{ M}_\odot \text{ pc}^{-2}$  are shown in Fig. 7. A single choice for the parameter  $\rho_B$  should, in principle, fit the total number of stars observed in each radial bin when we include all the stars at that location irrespective of their velocities. Unfortunately, this does not happen, and the observed number of stars, especially at galactocentric distances below  $\sim 20\text{-}30 \text{ kpc}$ , fall short of the theoretical expectation. The most likely explanation for this is that the samples of BS and BHB stars are incomplete in these regions. In fact, the radial distribution presented by Xue et al. (2008) and Brown et al. (2010) also differ significantly from each other. We therefore integrate  $4\pi r^2 F_B(r, v_r)$  over radial location and radial velocity,  $\Delta r(r_i)$  and  $\Delta v_r(r_i, v_j)$  respectively, and compare it with similarly binned observational data after normalizing the model estimates to the total number of stars observed in each individual bin separately. A selection of the fits are shown in Figs. 8 and 9 for the disk model with  $r_{tn} = 3.0 \text{ kpc}$  and  $\Sigma_{d,\odot} = 55 \text{ M}_\odot$ .

For finding out how well the different models fit the observations, we define  $f_{ij}$  as the theoretical expectation for the number of stars in the radial bin  $r_i$  and the velocity bin  $v_{rj}$ . If  $n_{ij}$  is the actual number of stars observed in this bin, then using Poisson statistics, we may define the likelihood function for each model to be

$$L = \prod_{ij} \frac{e^{-f_{ij}} f_{ij}^{n_{ij}}}{n_{ij}!}. \quad (25)$$

After the likelihoods for all the models were calculated, they were normalized to the model with the greatest likelihood, namely with  $\rho_{DM,c} = 100 \text{ GeV cm}^{-3}$ ,  $\sigma_{DM} = 220 \text{ km s}^{-1}$ ,  $\Sigma_{d,\odot} = 55 \text{ M}_\odot \text{ pc}^{-2}$ , and  $r_{tn} = 3.0 \text{ kpc}$ . The likelihood for each dark matter model that fits the rotation curve is show in the final rows of Tables 1-7.

Most of the models with high probability, according to the BHB and BS analysis, occur for  $\rho_{DM,c} \gtrsim 100 \text{ GeV cm}^{-3}$ . Also, except for two specific cases, one in each of the  $r_{tn} = 2.5$

and 3.5 kpc scenarios, the models with  $L > 0.7$  are found for the choice  $r_{tn} = 3.0$  kpc. All models with  $L > 0.8$  are found for  $r_{tn} = 3.0$  kpc and  $\Sigma_{d,\odot} = 55 \text{ M}_\odot \text{ pc}^{-2}$ . Most models for the  $r_{tn} = 3.5$  kpc disk, though they fit the rotation curve, do not predict enough stars at large velocities to agree with the BHB and BS data (Note the sharply falling rotation curves at large distances in these models.) and have a likelihood  $L = 0$ .

If we consider only the models with  $L > 0.7$ , we find the following range in the parameters for the dark matter particles in the Galaxy:

$$\begin{aligned}
 930.8 \text{ km s}^{-1} &\lesssim v_{esc}(0) \lesssim 983.9 \text{ km s}^{-1} \\
 597.1 \text{ km s}^{-1} &\lesssim v_{esc}(R_0) \lesssim 705.0 \text{ km s}^{-1} \\
 75 \text{ GeV cm}^{-3} &\lesssim \rho_{DM,c} \lesssim 500 \text{ GeV cm}^{-3} \\
 0.395 \text{ GeV cm}^{-3} &\lesssim \rho_{DM}(R_0) \lesssim 0.758 \text{ GeV cm}^{-3} \\
 462.5 \text{ km s}^{-1} &\lesssim \langle v_{DM}^2(R_0) \rangle^{1/2} \lesssim 546.1 \text{ km s}^{-1} \\
 1.60 \times 10^{12} \text{ M}_\odot &\lesssim M_{Galaxy} \lesssim 2.00 \times 10^{12} \text{ M}_\odot.
 \end{aligned}$$

## 6. Discussion

While the observations of the rotation curve remain the best probes of the Galactic potential out to  $\sim 20$  kpc, the high dispersion in the observed rotation speeds, especially at large distances, does not allow a precise determination of the parameters characterizing the phase-space distribution of Galactic dark matter. Among the models where the rotation curve is confined to lie within a narrow band encompassing 2/3 of the observed data, a wide range in the parameters is allowed, as shown in Tables 1-7 and Figs. 3-6. It may be possible to further constrain the dark matter phase-space distribution by comparing the vertical force exerted by the Galactic potential at  $R_0$  displayed for several models in Fig.

6 with the stellar observations perpendicular to the plane in the Solar neighborhood as an extension of the analysis by Kuijken & Gilmore (1989).

The model providing the best fit for disks with surface densities within observational constraints to both the rotation curve and the BHB/BS distributions occurs for the following dark matter phase-space distribution parameters:  $\rho_{DM,c}=100 \text{ GeV cm}^{-3}$ ,  $\Psi_0/\sigma_{DM}^2=10$ , and  $\sigma_{DM} = 220 \text{ km s}^{-1}$ . The corresponding properties of the dark matter relevant to its direct detection are  $\langle v^2(R_0)_{DM} \rangle^{1/2} \approx 546 \text{ km s}^{-1}$  and  $\rho_{DM}(R_0) \approx 0.72 \text{ GeV cm}^{-3}$ . This local dark matter density is notably higher than the currently adopted Standard Halo Model. The effect this increase has on the expected rates of direct and indirect detection predictions will be discussed in a companion paper.

Better observations of the distance of the Sun from the Galactic center and the value of the rotation speed at the Solar circle as well as observations of the rotation curve beyond  $R_0$ , especially at distances beyond 20 kpc, would allow for better constraints on the phase-space distribution of dark matter. The currently observed distributions of BHB and BS stars have large uncertainties as to their absolute spatial densities and do not place tight bounds on the dark matter phase-space distribution on their own. This was shown by the wide range of dark matter models that adequately reproduced the velocity distributions at various distances compiled by Xue et al. and Brown et al. The wide range of allowed parameters shows that more precise astronomical observations, especially pertaining to the surface mass density of the disk and its radial scale length, are needed to narrow down the parameters of the phase-space distribution of dark matter and to be able to correctly interpret the results of direct and indirect dark matter detection experiments. As far as the present status of the observations are concerned, assuming the surface density of the Galactic disk is  $\sim 55 \text{ M}_\odot \text{ pc}^{-2}$ , a value in the middle of the observational constraints, and a thin disk scale length of 3.0 kpc, the best choice for the parameters of Galactic dark matter

(Li0.7) are the following:  $\rho_{DM,c} \approx 100 - 250 \text{ GeV cm}^{-3}$ ,  $\rho_{DM}(R_0) \approx 0.56 - 0.72 \text{ GeV cm}^{-3}$ , and  $\langle v_{DM}^2(R_0) \rangle^{1/2} \approx 490\text{--}550 \text{ km s}^{-1}$ , which yield a total mass of the Galaxy including the dark matter halo of  $M_{Galaxy} \approx 1.68 - 2.00 \times 10^{12} \text{ M}_{\odot}$ .

## REFERENCES

- Aghmet, Z., et al. 2011, PRL, 106, 131302
- Aprile, E., et al. 2012, PRL, 109, 181301
- Archambault, S. et al. 2012, Phys. Lett. B, 711, 153
- Avedisova, V.S. 2005, Astron. Rep., 49, 435
- Bahcall, J. N. & Soneira, R. M. 1980, ApJ Sup. Ser., 44, 73
- Behnke et al. 2011, Phys. Rev. Lett., 106, 021303
- Bensby, T. et al. 2011, ApJ, 735, L46
- Bhattacharjee, P. et al. 2013, Phys. Rev. D, 87, 083525
- Binney, J. & Tremaine, S. 2008, Galactic Dynamics, (2nd ed; Princeton, NJ: Princeton, University Press)
- Blitz, L., Fich, M., & Stark, A. A. 1982, ApJS, 49, 183
- Blum, R. D., et al. 1995, ApJ, 449, 623
- Bovy, J. & Tremaine, S. 2012, AJ, 756, 89
- Bovy, J. et al. 2012a, ApJ, 753, 148
- Bovy, J. et al. 2012b, ApJ, 759, 131
- Brown, W. R., et al. 2010, ApJ, 139, 59
- Brunthaler, A., et al. 2011, Astron. Nachr., 332, 461
- Burton, W. B. & Gordon, M. A. 1978,  $\alpha$ , 63, 7

- Burton, W. B. & Liszt, H. S. 1993, *Å*, 274, 765
- Buser, R., Rong, J., & Karaali, S. 1999, *Å*, 348, 98
- Cabrera-Lavers, A., Garzón, F., & Hammersley, P. L. 2005, *Å*, 433, 173
- Caldwell, J. A. R. & Ostriker, J. P. 1981, *AJ*, 251, 61
- Carollo, D., et al. 2010, *ApJ*, 712, 692
- Catena, R. & Ullio, P. 2010, *JCAP*, 08, 004
- Catena, R. & Ullio, P. 2012, *JCAP*, 05, 005
- Chaudhury, S., Bhattacharjee, P., & Cowsik, R. 2010, *JCAP*, 09, 020
- Cheng, J. Y. et al. 2012, *ApJ*, 752, 51
- Clemens, D. P. 1985, *ApJ*, 295, 422
- Cowsik, R., Ratnam, C., & Bhattacharjee, P. 1996, *Phys. Rev. Lett.*, 76, 3886
- Cowsik, R. & McClelland, J. 1972, *PRL*, 29, 669
- Cowsik, R. & McClelland, J. 1973, *ApJ*, 180, 7
- Cowsik, R., et al. 2007, *New A*, 12, 507
- Dehnen, W. & Binney, J. 1998, *MNRAS*, 294, 429
- Dejonghe, H. 1987, *MNRAS*, 224, 12
- Demers, S. & Battinelli, P. 2007, *Å*, 473, 143
- Felizardo, M. et al. 2012, *Phys. Rev. Lett.*, 108, 201302
- Fich, M., Blitz, L., & Stark, A. A. 1989, *ApJ*, 342, 272

- Flynn, C. & Fuchs, B. 1994, MNRAS, 270, 471
- Flynn, C., et al. 2006, MNRAS, 372, 1149
- Freeman, K. C. 1970, ApJ, 160, 811
- Ghez, A. M., et al. 2008, ApJ, 689, 1044
- Gillessen, S., et al. 2009, ApJ, 692, 1075
- Gould, A., Bahcall, J. N., & Flynn, C. 1996, ApJ, 465, 759
- Helmi, A. 2008, A&AR, 15, 145
- Holmberg, J. & Flynn, C. 2004, MNRAS, 352, 440
- Honma, M. & Sofue, Y. 1997, PASJ, 49, 453
- Honma, M., et al. 2007, PASJ, 59, 889
- Jurić, M., et al. 2008, ApJ, 673, 864
- Kolb, E. & Turner, M. 1990, The Early Universe (Redwood City, CA: Addison-Wesley)
- Koposov, S. E. et al. 2010, ApJ, 712, 260
- Korchagin, V. I., et al. 2003, apj, 126, 2896
- Kuhlen, M. et al. 2010, JCAPJCAP, 02, 030
- Kuijken, K. & Gilmore, G. 1989, MNRAS, 239, 605
- Kuijken, K. & Gilmore, G. 1991, ApJ, 367, L9
- Larsen, J. A. & Humphreys, R. M. 2003, AJ, 125, 1958
- Lee, B. W. & Weinberg, S. 1977, Phys. Rev. Lett., 39, 165



- Libeskind, N. I. et al., 2010, MNRAS, 411, 1525
- McClure-Griffiths, N. M. & Dickey, J. M. 2007, ApJ, 671, 427
- McMillan, P. J. & Binney, J. J. 2010, MNRAS, 402, 934
- McMillan, P. J. 2011, MNRAS, 414, 2446
- Minniti, D., et al. 1992, ApJ, 393, L47
- Mo, H., van den Bosch, F., & White, S. 2010, Galaxy Formation and Evolution, (Cambridge: Cambridge University Press)
- Navarro, J. F., Frenk, C. S., & White, S. D. M. 1997, ApJ, 490, 493
- Nesti, F. and Salucci, P. 2013, arXiv:1304.5127v2
- Ng, Y. K., et al. 1997, Å, 324, 65
- Oh, C. S., et al. 2010, PASJ, 62, 101
- Ojha, D. K. 2001, MNRAS, 322, 426
- Oort, J. 1932, Bull. Astron. Inst. Neth., 6, 249
- Pont, F., et al. 1997, Å, 318, 416
- Prendergast, K. H. & Tomer, E. 1970, AJ, 75, 674
- Reid, M. J. & Brunthaler, A. 2004, ApJ, 616, 872
- Reid, M. J., et al. 2008, ApJ, 700, 137
- Reid, M. J. 2009, Int. J. Mod. Phys. D, 18, 889
- Reid, N. & Majewski, S. R. 1993, ApJ, 409, 635

- Rich, M., et al. 2007, *ApJ*, 658, L29
- Robin, A. C., et al. 1996, *å*, 305, 125
- Rohlfs, K. & Kreitschmann, J. 1988, *å*, 201, 51
- Salucci, P. et al. 2010, *å*, 523, 83
- Schmidt, M. 1956, *Bull. Artron. Inst. Neth.*, 13, 15
- Bahcall, J. N., Schmidt, M., & Soneira, R. M. 1983, *AJ*, 265, 730
- Schneider, S. E. & Terzian, Y. 1983, *ApJ*, 274, L61
- Schönrich, R., Binney, J. & Dehnen, W. 2010, *MNRAS*, 403, 1829
- Siebert, A., Bienaymé, O, and Soubiran, C. 2003, *å*, 399, 531
- Siegel, M. H., et al. 2002, *ApJ*, 578, 151
- Sofue, Y., Honma, M., & Omodaka, T. 2009, *PASJ*, 61, 227
- Spagna, A., et al. 1996, *å*, 313, L21
- Stepanishchev, A. S. & Bobylev, V. V. 2011, *Astron. Lett.*, 37, 254
- Turbide, L. & Moffat, A. F. J. 1993, *AJ*, 105, 1831
- Weber, W. & de Boer, W. 2010, *å*, 509, A25
- Wilson, C. P. 1975, *ApJ*, 80, 175
- Xue, X. X., et al. 2008, *ApJ*, 684, 1143

Table 1: Models for the  $r_{tn} = 2.5$  and  $\Sigma_{d,\odot}=40 \text{ M}_\odot \text{ pc}^{-2}$  disk.

$\rho_{DM,c} [\text{GeV cm}^{-3}]$	25	50	75	100	250	500
$\sigma_{DM} [\text{km s}^{-1}]$	–	240	225	220	205	–
			230	225		
$\Psi_0/\sigma_{DM}^2$	–	8	9	9	10	–
			9	9		
$v_{esc}(0) [\text{km s}^{-1}]$	–	960	955	933	917	–
			976	955		
$v_c(R_0) [\text{km s}^{-1}]$	–	246	241	242	243	–
			250	252		
$\langle v_{DM}^2(R_0) \rangle^{1/2} [\text{km s}^{-1}]$	–	522	515	487	454	–
			534	506		
$\rho_{DM}(R_0) [\text{GeV cm}^{-3}]$	–	0.723	0.644	0.632	0.573	–
			0.737	0.726		
$v_{esc}(R_0) [\text{km s}^{-1}]$	–	673	665	629	586	–
			689	653		
$M_{galaxy} [10^{12} \text{ M}_\odot]$	–	1.54	1.64	1.34	1.10	–
			1.71	1.40		
$L [\text{km s}^{-1}]$	–	0.274	0.652	0.093	0	–
			0.746	0.173		

Table 2: Models for the  $r_{tn} = 3.0$  and  $\Sigma_{d,\odot}=40 \text{ M}_\odot \text{ pc}^{-2}$  disk.

$\rho_{DM,c} [\text{GeV cm}^{-3}]$	25	50	75	100	250	500
$\sigma_{DM} [\text{km s}^{-1}]$	–	–	–	–	205	195
$\Psi_0/\sigma_{DM}^2$	–	–	–	–	11	12
$v_{esc}(0) [\text{km s}^{-1}]$	–	–	–	–	962	955
$v_c(R_0) [\text{km s}^{-1}]$	–	–	–	–	250	244
$< v_{DM}^2(R_0) >^{1/2} [\text{km s}^{-1}]$	–	–	–	–	515	498
$\rho_{DM}(R_0) [\text{GeV cm}^{-3}]$	–	–	–	–	0.760	0.662
$v_{esc}(R_0) [\text{km s}^{-1}]$	–	–	–	–	665	643
$M_{galaxy} [10^{12} \text{ M}_\odot]$	–	–	–	–	1.61	1.62
$L [\text{km s}^{-1}]$	–	–	–	–	0.777	0.791

Table 3: Models for the  $r_{tn} = 3.0$  and  $\Sigma_{d,\odot}=55 \text{ M}_{\odot} \text{ pc}^{-2}$  disk.

$\rho_{DM,c} [\text{GeV cm}^{-3}]$	25	50	75	100	250	500
$\sigma_{DM} [\text{km s}^{-1}]$	–	–	–	220	200	195
	–	–	–	–	205	–
$\Psi_0/\sigma_{DM}^2$	–	–	–	10	11	11
	–	–	–	–	11	–
$v_{esc}(0) [\text{km s}^{-1}]$	–	–	–	984	938	915
	–	–	–	–	962	–
$v_c(R_0) [\text{km s}^{-1}]$	–	–	–	251	241	245
	–	–	–	–	252	–
$\langle v_{DM}^2(R_0) \rangle^{1/2} [\text{km s}^{-1}]$	–	–	–	546	489	443
	–	–	–	–	508	–
$\rho_{DM}(R_0) [\text{GeV cm}^{-3}]$	–	–	–	0.719	0.563	0.535
	–	–	–	–	0.654	–
$v_{esc}(R_0) [\text{km s}^{-1}]$	–	–	–	705	631	571
	–	–	–	–	656	–
$M_{galaxy} [10^{12} \text{ M}_{\odot}]$	–	–	–	2.00	1.60	1.06
	–	–	–	–	1.68	–
$L [\text{km s}^{-1}]$	–	–	–	1	0.732	0
	–	–	–	–	0.834	–

Table 4: Models for the  $r_{tn} = 3.0$  and  $\Sigma_{d,\odot}=70 \text{ M}_\odot \text{ pc}^{-2}$  disk.

$\rho_{DM,c} [\text{GeV cm}^{-3}]$	25	50	75	100	250	500
$\sigma_{DM} [\text{km s}^{-1}]$	255	235	220	215	200	190
$\Psi_0/\sigma_{DM}^2$	7	8	9	9	11	12
$v_{esc}(0) [\text{km s}^{-1}]$	954	940	933	912	938	931
$v_c(R_0) [\text{km s}^{-1}]$	244	248	243	243	246	241
$< v_{DM}^2(R_0) >^{1/2} [\text{km s}^{-1}]$	520	498	491	463	481	463
$\rho_{DM}(R_0) [\text{GeV cm}^{-3}]$	0.573	0.582	0.505	0.489	0.470	0.395
$v_{esc}(R_0) [\text{km s}^{-1}]$	671	643	634	598	621	597
$M_{galaxy} [10^{12} \text{ M}_\odot]$	1.69	1.46	1.58	1.27	1.67	1.69
$L [\text{km s}^{-1}]$	0.524	0.250	0.597	0.056	0.784	0.764

Table 5: Models for the  $r_{tn} = 3.5$  and  $\Sigma_{d,\odot}=40 \text{ M}_\odot \text{ pc}^{-2}$  disk.

$\rho_{DM,c} [\text{GeV cm}^{-3}]$	25	50	75	100	250	500
$\sigma_{DM} [\text{km s}^{-1}]$	–	–	–	–	–	200
$\Psi_0/\sigma_{DM}^2$	–	–	–	–	–	10
$v_{esc}(0) [\text{km s}^{-1}]$	–	–	–	–	–	894
$v_c(R_0) [\text{km s}^{-1}]$	–	–	–	–	–	251
$< v_{DM}^2(R_0) >^{1/2} [\text{km s}^{-1}]$	–	–	–	–	–	421
$\rho_{DM}(R_0) [\text{GeV cm}^{-3}]$	–	–	–	–	–	0.736
$v_{esc}(R_0) [\text{km s}^{-1}]$	–	–	–	–	–	544
$M_{galaxy} [10^{12} \text{ M}_\odot]$	–	–	–	–	–	0.67
$L [\text{km s}^{-1}]$	–	–	–	–	–	0

Table 6: Models for the  $r_{tn} = 3.5$  and  $\Sigma_{d,\odot}=55 \text{ M}_\odot \text{ pc}^{-2}$  disk.

$\rho_{DM,c} [\text{GeV cm}^{-3}]$	25	50	75	100	250	500
$\sigma_{DM} [\text{km s}^{-1}]$	–	–	–	–	205	195
$\Psi_0/\sigma_{DM}^2$	–	–	–	–	11	11
$v_{esc}(0) [\text{km s}^{-1}]$	–	–	–	–	962	915
$v_c(R_0) [\text{km s}^{-1}]$	–	–	–	–	254	246
$< v_{DM}^2(R_0) >^{1/2} [\text{km s}^{-1}]$	–	–	–	–	515	450
$\rho_{DM}(R_0) [\text{GeV cm}^{-3}]$	–	–	–	–	0.758	0.631
$v_{esc}(R_0) [\text{km s}^{-1}]$	–	–	–	–	665	581
$M_{galaxy} [10^{12} \text{ M}_\odot]$	–	–	–	–	1.61	1.02
$L [\text{km s}^{-1}]$	–	–	–	–	0.781	0

Table 7: Models for the  $r_{tn} = 3.5$  and  $\Sigma_{d,\odot}=70 \text{ M}_\odot \text{ pc}^{-2}$  disk.

$\rho_{DM,c} [\text{GeV cm}^{-3}]$	25	50	75	100	250	500
$\sigma_{DM} [\text{km s}^{-1}]$	–	–	–	225	200	195
	–	–	–	–	205	–
$\Psi_0/\sigma_{DM}^2$	–	–	–	8	10	10
	–	–	–	–	10	–
$v_{esc}(0) [\text{km s}^{-1}]$	–	–	–	900	894	872
	–	–	–	–	917	–
$v_c(R_0) [\text{km s}^{-1}]$	–	–	–	256	243	245
	–	–	–	–	254	–
$\langle v_{DM}^2(R_0) \rangle^{1/2} [\text{km s}^{-1}]$	–	–	–	451	441	392
	–	–	–	–	459	–
$\rho_{DM}(R_0) [\text{GeV cm}^{-3}]$	–	–	–	0.725	0.551	0.502
	–	–	–	–	0.642	–
$v_{esc}(R_0) [\text{km s}^{-1}]$	–	–	–	582	569	506
	–	–	–	–	593	–
$M_{galaxy} [10^{12} \text{ M}_\odot]$	–	–	–	0.84	0.98	1.04
	–	–	–	–	0.61	–
$L [\text{km s}^{-1}]$	–	–	–	0	0	0
	–	–	–	–	0	–



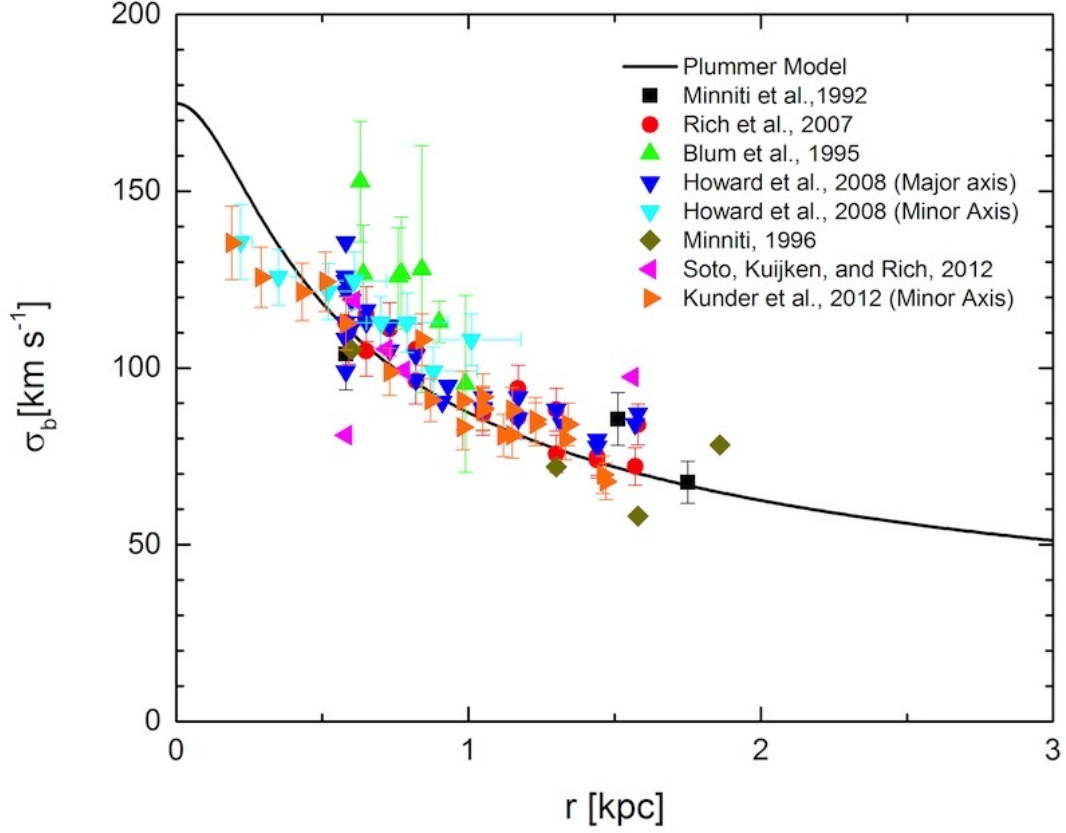


Fig. 1.— The velocity dispersion expected from the bulge (eq. 10) is plotted along with K and M giant observations (Minniti 1992; Rich et al. 2007; Blum et al. 1995). The agreement between the observations and the prediction from the Plummer profile implies that the mass distribution of the bulge can be adequately fit by a Plummer profile in the region of interest.

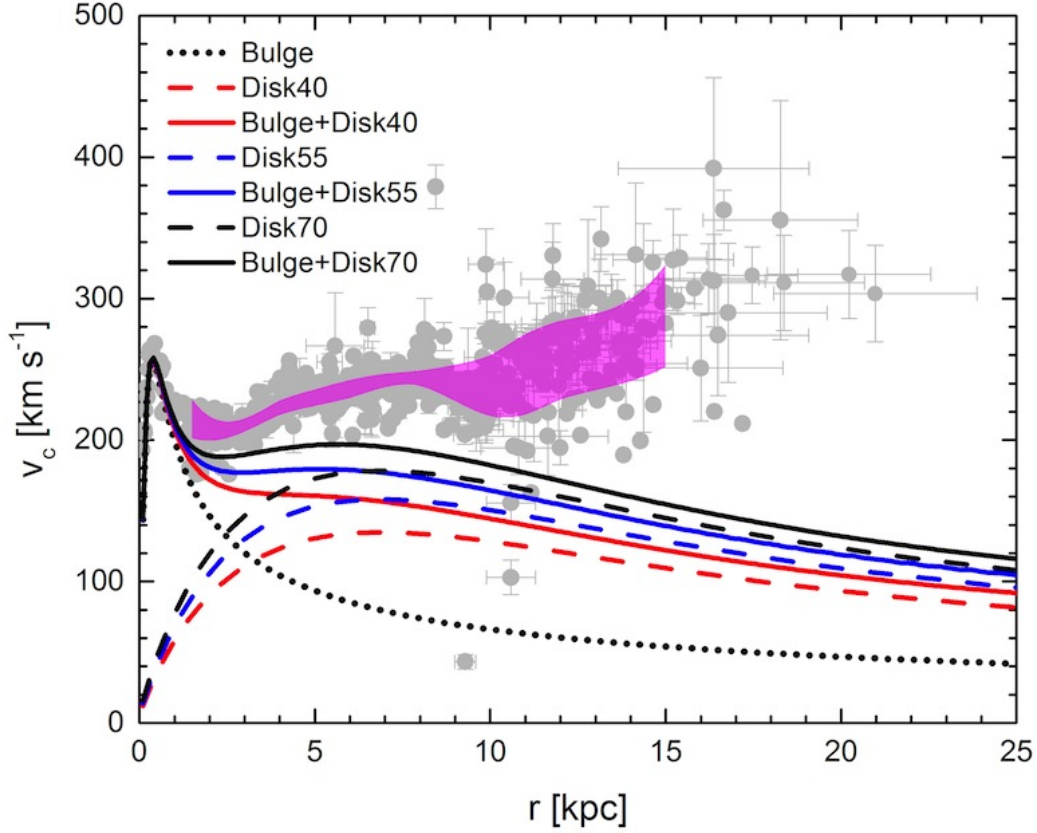


Fig. 2.— Observations of the rotation curve (Burton & Gordon 1978; Blitz et al. 1982; Schneider & Terzian 1983; Clemens 1985; Fich et al. 1989; Burton & Liszt 1993; Turbide & Moffat 1993; Honma & Sofue 1997; Pont et al. 1997; Honma et al. 2007; McClure-Griffiths & Dickey 2007; Oh et al. 2010; Stepanishchev & Bobylev 2011) are plotted after rescaling all the data using  $R_0 = 8.3$  kpc and  $\Theta_0 = 240$  km s $^{-1}$  and adjusting for the current measurements of the peculiar motion of the Sun. The magenta band indicates there region where 2/3 of the points lie within 1 kpc radial bins. The rotation curve predicted by the visible matter components alone for the three local disk surface densities with  $r_{tn} = 3.0$  kpc is shown along with the shaded observations.

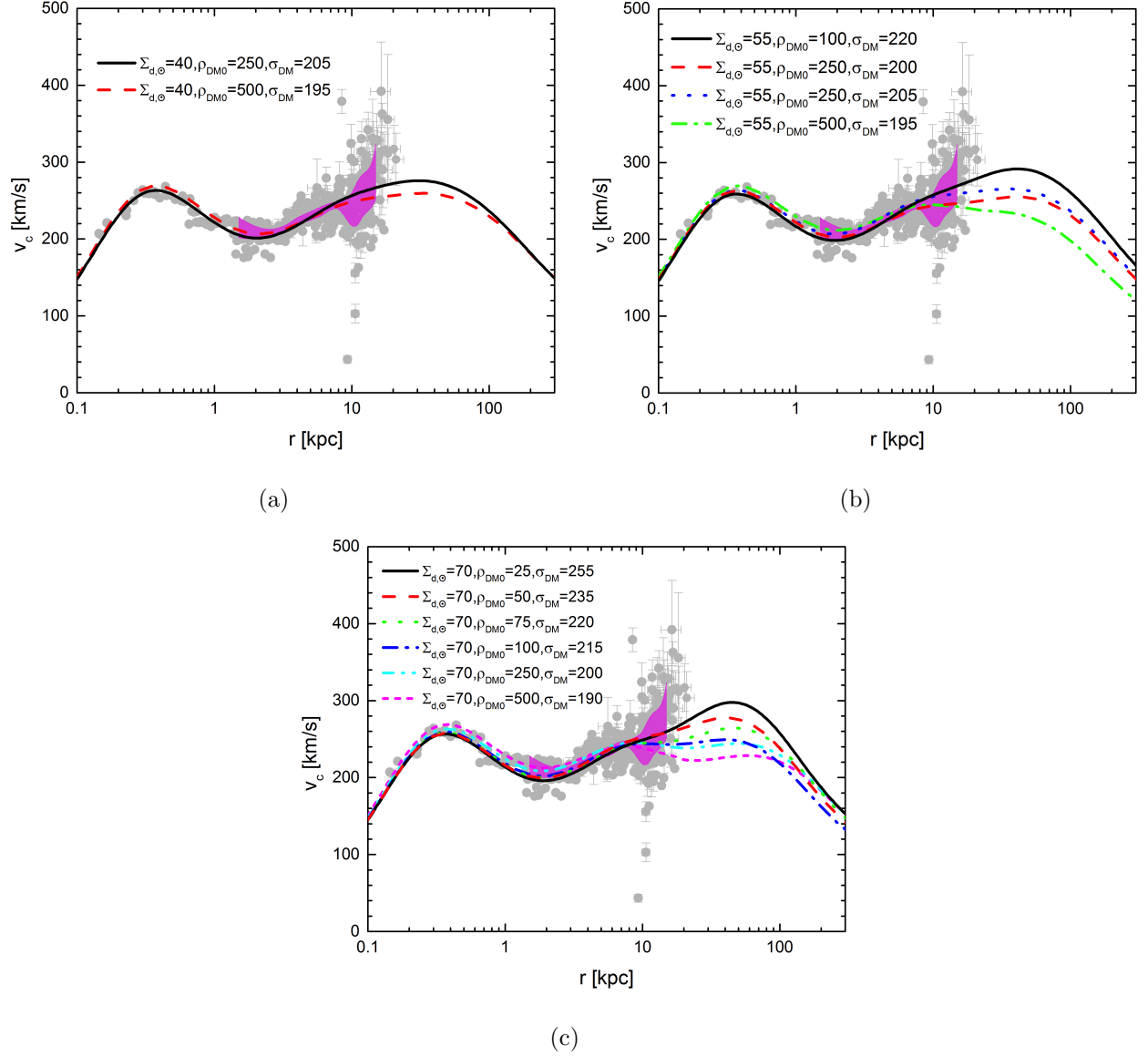


Fig. 3.— The rotation curves are shown for the dark matter models which pass through the band encompassing 2/3 of the observations in 1 kpc bins for  $r_{tn} = 3.0$  kpc and (a)  $\Sigma_{d,\odot} = 40 \text{ M}_\odot \text{ pc}^{-2}$ , (b)  $\Sigma_{d,\odot} = 55 \text{ M}_\odot \text{ pc}^{-2}$ , and (c)  $\Sigma_{d,\odot} = 70 \text{ M}_\odot \text{ pc}^{-2}$

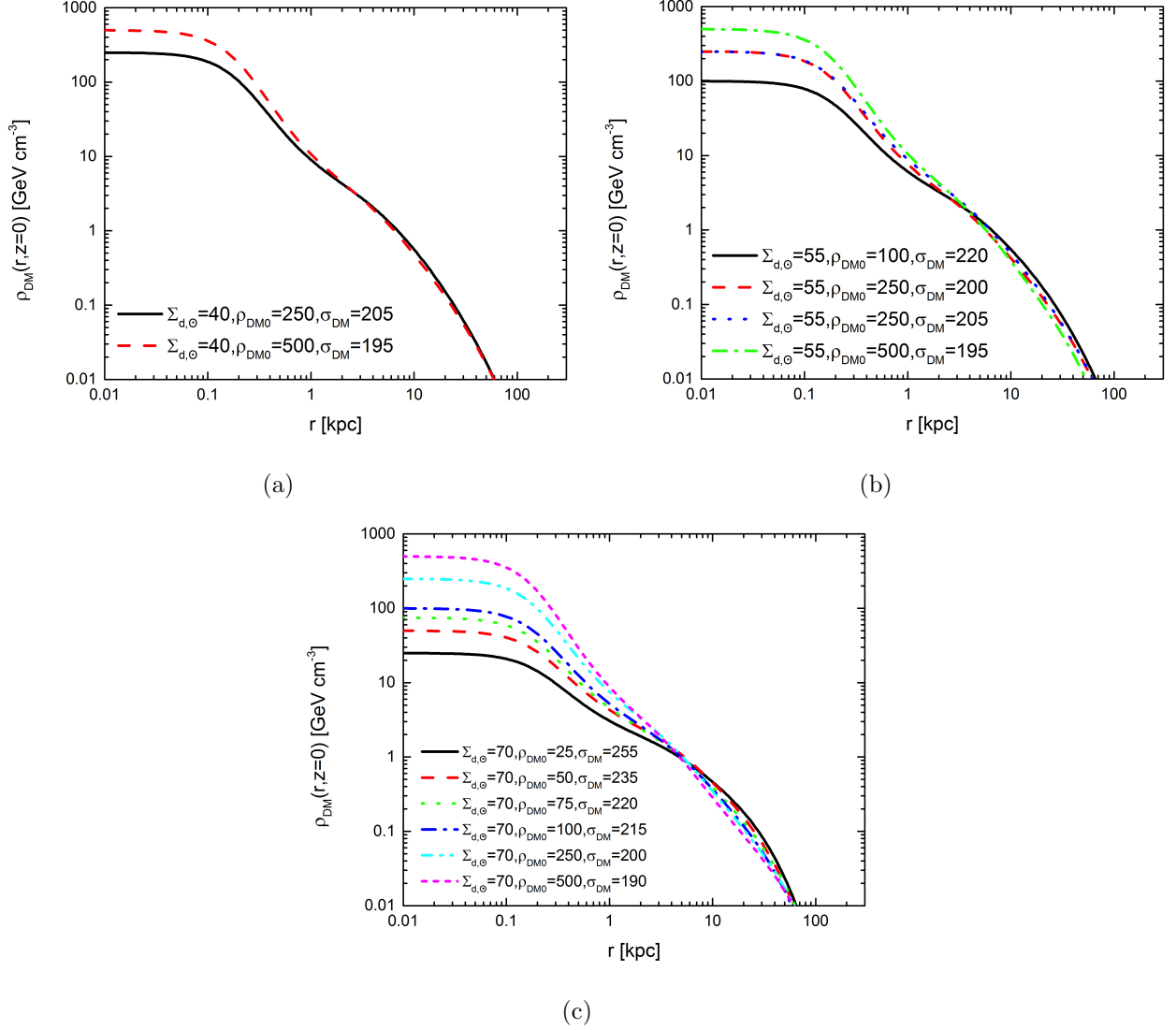


Fig. 4.— The density profiles for dark matter models which best fit the rotation curve are shown for  $r_{\text{tn}}$  and: (a)  $\Sigma_{d,\odot} = 40 \text{ M}_\odot \text{ pc}^{-2}$ , (b)  $\Sigma_{d,\odot} = 55 \text{ M}_\odot \text{ pc}^{-2}$ , and (c)  $\Sigma_{d,\odot} = 70 \text{ M}_\odot \text{ pc}^{-2}$ .

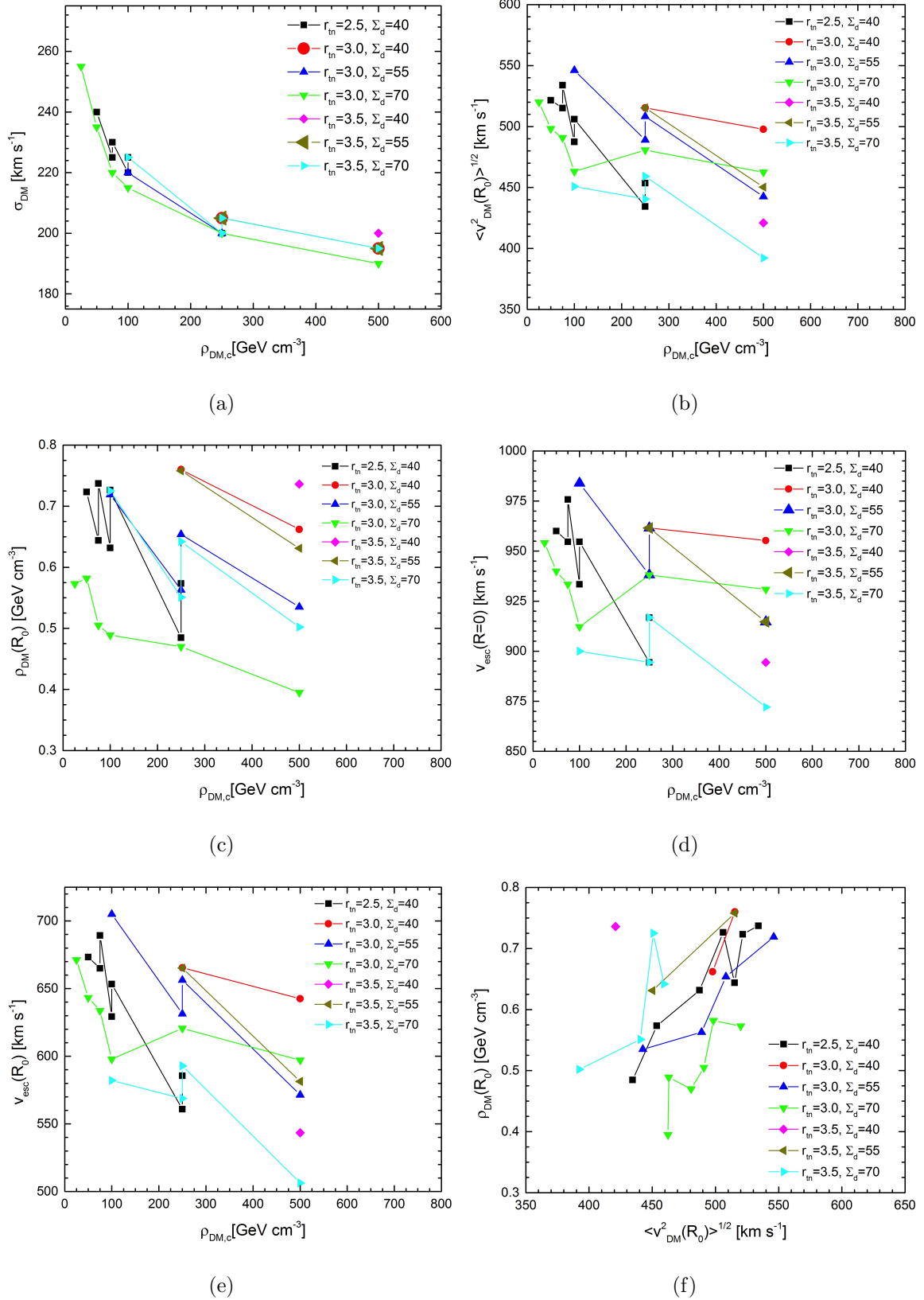


Fig. 5.— The correlation between the various model parameters of dark matter that fit the rotation curve of the Galaxy.

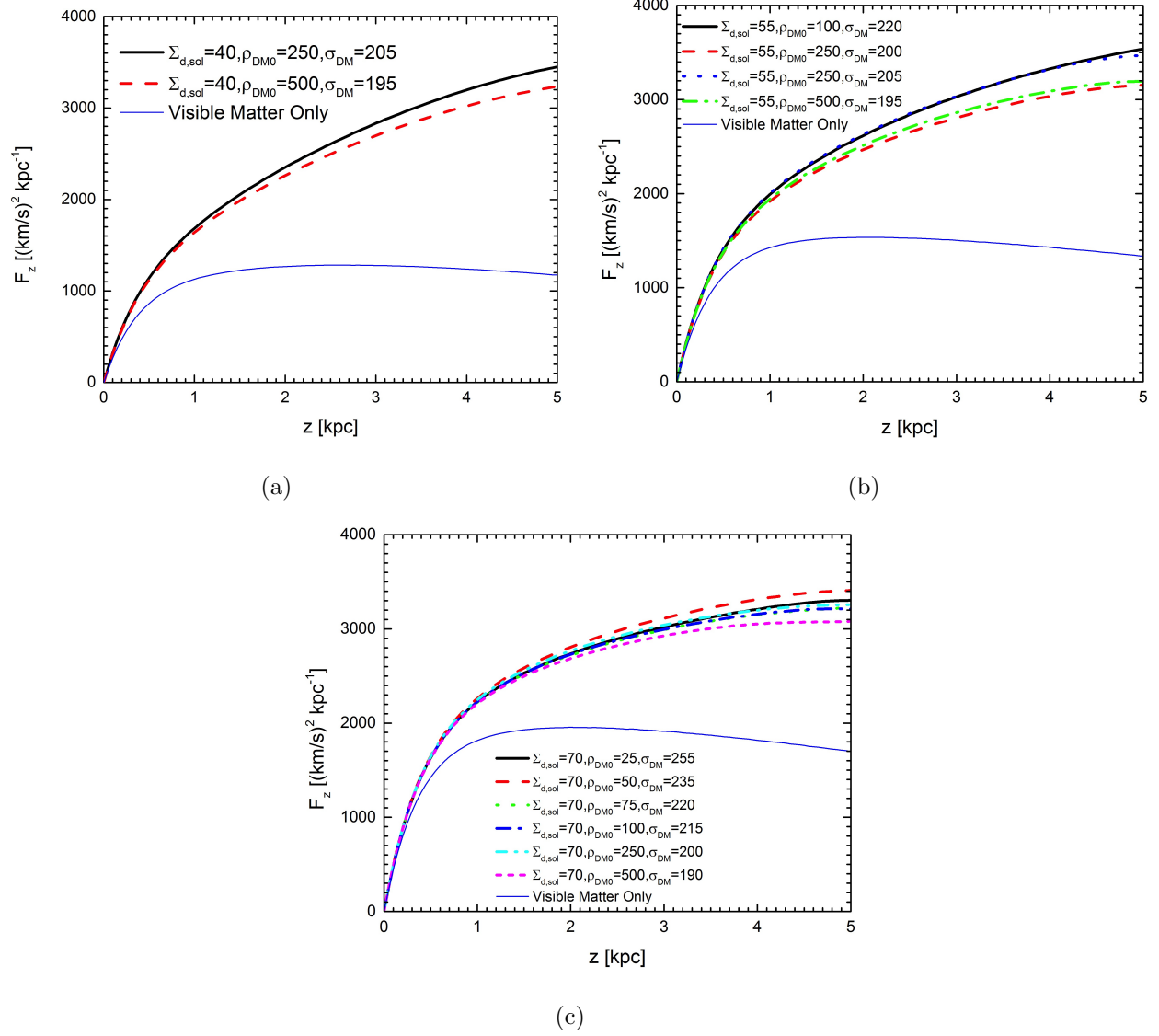


Fig. 6.— The vertical force profiles at the galactocentric distance of the Sun for dark matter models which best fit the rotation curve are shown for  $r_{tn} = 3.0 \text{ kpc}$  and: (a)  $\Sigma_{d,\odot} = 40 \text{ M}_\odot \text{ pc}^{-2}$ , (b)  $\Sigma_{d,\odot} = 55 \text{ M}_\odot \text{ pc}^{-2}$ , and (c)  $\Sigma_{d,\odot} = 70 \text{ M}_\odot \text{ pc}^{-2}$ .

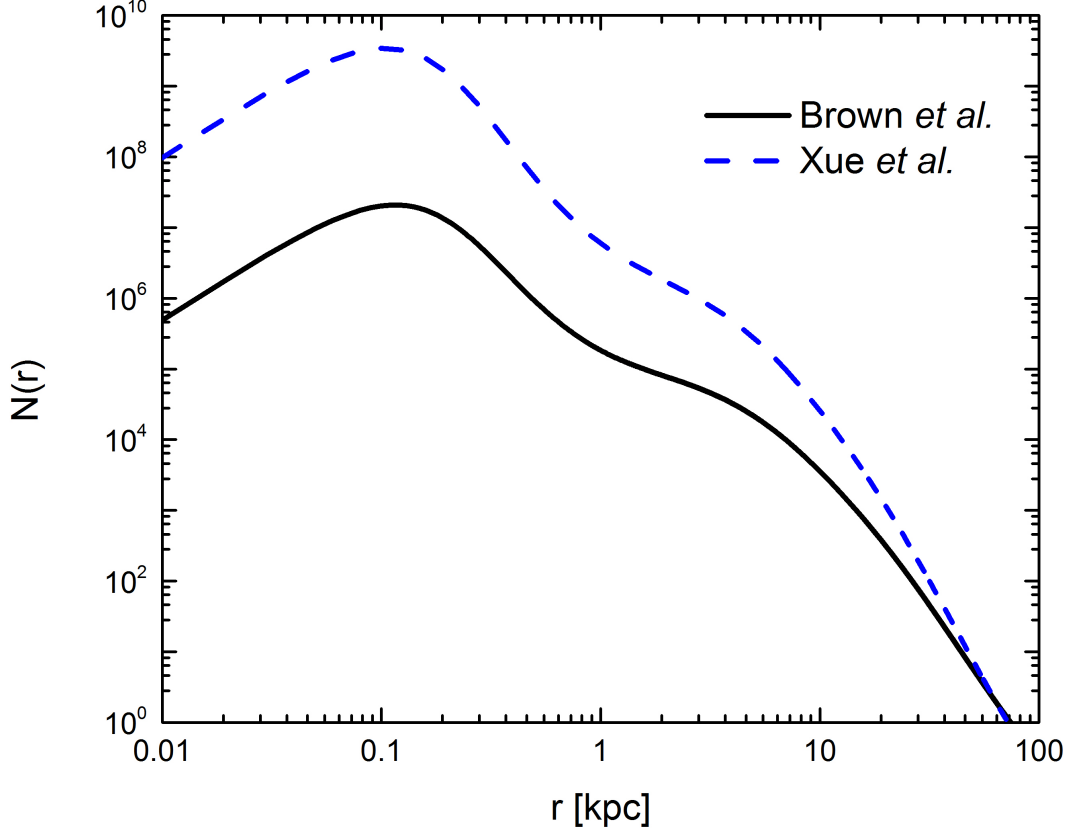


Fig. 7.— The theoretical radial distribution of BHB and BS stars expected from the velocity distribution measured by Brown et al. and Xue et al. The distribution is shown for the  $\Sigma_{d,\odot}=55 \text{ M}_{\odot} \text{ pc}^{-2}$ ,  $r_{tn} = 3.0 \text{ kpc}$  disk with  $\rho_{DM,c} = 100 \text{ GeV cm}^{-3}$ ,  $\sigma_{DM} = 220 \text{ km s}^{-1}$ , and  $\sigma_{BHB} = \sigma_{BS} = 115 \text{ km s}^{-1}$  for Brown et al. and  $\sigma_{BHB} = 106 \text{ km s}^{-1}$  for Xue et al.

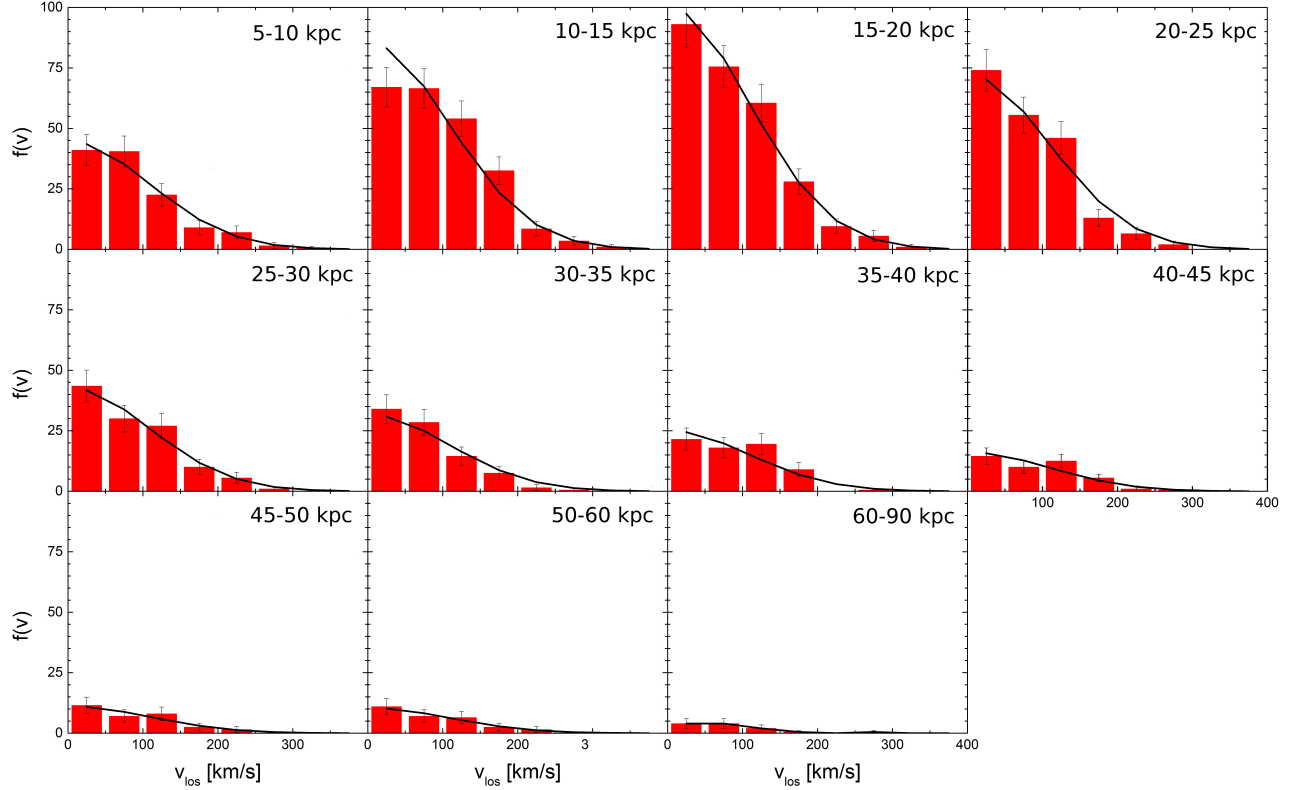


Fig. 8.— The line-of-sight velocity distribution of BHB stars from Xue et al. (2008) is presented in radial velocity and radial bins in the red histogram with error bars. The distribution computed for the best-fit dark matter model for the  $\Sigma_{d,\odot}=55 \text{ M}_{\odot} \text{ pc}^{-2}$ ,  $r_{tn} = 3.0$  kpc, disk is shown as points, connected for clarity. In this model,  $\rho_{DM,c} = 100 \text{ GeV cm}^{-3}$ ,  $\sigma_{DM} = 220 \text{ km s}^{-1}$ ,  $\Phi_0/\sigma_{DM}^2=10$  and  $\sigma_{BHB} = 106 \text{ km s}^{-1}$ .



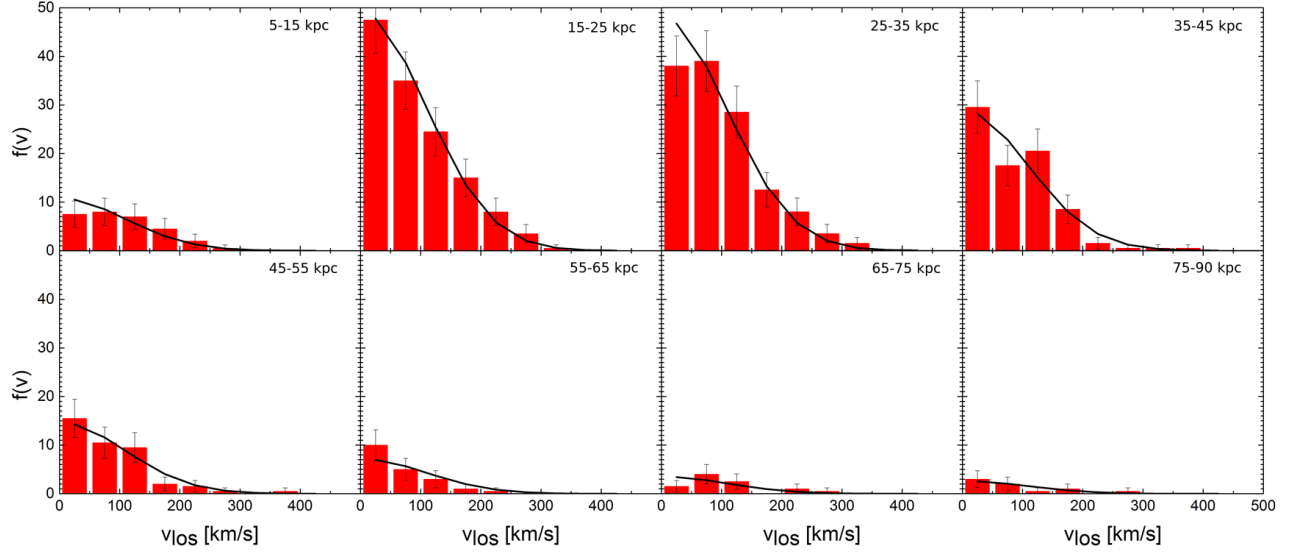


Fig. 9.— The line-of-sight velocity distribution of BHB and BS stars from Brown et al. (2010) is presented in radial velocity and radial bins in the red histogram with error bars. The distribution computed for the best-fit dark matter model for the  $\Sigma_{d,\odot}=55 \text{ M}_{\odot} \text{ pc}^{-2}$ ,  $r_{tn} = 3.0 \text{ kpc}$  disk is shown as points, connected for clarity. In this model,  $\rho_{DM,c} = 200 \text{ GeV cm}^{-3}$ ,  $\sigma_{DM} = 230 \text{ km s}^{-1}$ ,  $\Phi_0/\sigma_{DM}^2=10$  and  $\sigma_{BHB,BS} = 115 \text{ km s}^{-1}$ .